Optical modeling of plasma-deposited ZnO films : electron scattering at different length scales

JVSTA Journal of Vacuum Science & Technology A

Optical modeling of plasma-deposited ZnO films: Electron scattering at different length scales

Harm C. M. Knoops, Bas W. H. van de Loo, Sjoerd Smit, Mikhail V. Ponomarev, Jan-Willem Weber, Kashish Sharma, Wilhelmus M. M. Kessels, and Mariadriana Creatore

Citation: Journal of Vacuum Science & Technology A **33**, 021509 (2015); doi: 10.1116/1.4905086
View online: http://dx.doi.org/10.1116/1.4905086
View Table of Contents: http://scitation.aip.org/content/avs/journal/jvsta/33/2?ver=pdfcov
Published by the AVS: Science & Technology of Materials, Interfaces, and Processing

Optical modeling of plasma-deposited ZnO films: Electron scattering at different length scales

Harm C. M. Knoops,[a] Bas W. H. van de Loo, Sjoerd Smit, Mikhail V. Ponomarev, Jan-Willem Weber, and Kashish Sharma
Department of Applied Physics, Eindhoven University of Technology, P.O. Box 513, 5600 MB Eindhoven, The Netherlands

Wilhelmus M. M. Kessels and Mariadriana Creatore[b]
Department of Applied Physics, Eindhoven University of Technology, P.O. Box 513, 5600 MB Eindhoven, The Netherlands and Solliance, High Tech Campus 5, 5656 AE Eindhoven, The Netherlands

(Received 18 September 2014; accepted 16 December 2014; published 31 December 2014)

In this work, an optical modeling study on electron scattering mechanisms in plasma-deposited ZnO layers is presented. Because various applications of ZnO films pose a limit on the electron carrier density due to its effect on the film transmittance, higher electron mobility values are generally preferred instead. Hence, insights into the electron scattering contributions affecting the carrier mobility are required. In optical models, the Drude oscillator is adopted to represent the free-electron contribution and the obtained optical mobility can be then correlated with the macroscopic material properties. However, the influence of scattering phenomena on the optical mobility depends on the considered range of photon energy. For example, the grain-boundary scattering is generally not probed by means of optical measurements and the ionized-impurity scattering contribution decreases toward higher photon energies. To understand this frequency dependence and quantify contributions from different scattering phenomena to the mobility, several case studies were analyzed in this work by means of spectroscopic ellipsometry and Fourier transform infrared (IR) spectroscopy. The obtained electrical parameters were compared to the results inferred by Hall measurements. For intrinsic ZnO (i-ZnO), the in-grain mobility was obtained by fitting reflection data with a normal Drude model in the IR range. For Al-doped ZnO (Al:ZnO), besides a normal Drude fit in the IR range, an Extended Drude fit in the UV-vis range could be used to obtain the in-grain mobility. Scattering mechanisms for a thickness series of Al:ZnO films were discerned using the more intuitive parameter "scattering frequency" instead of the parameter "mobility". The interaction distance concept was introduced to give a physical interpretation to the frequency dependence of the scattering frequency. This physical interpretation furthermore allows the prediction of which Drude models can be used in a specific frequency range.
 [http://dx.doi.org/10.1116/1.4905086]

I. INTRODUCTION

Thin films of polycrystalline zinc oxide (ZnO) are widely used in solar cells and other optoelectronic applications due to their transparency and electrical conductivity.[1] To be able to fulfill their potential, the optical and electrical properties of ZnO have to be understood and controlled. Especially, the electron carrier density N and electron mobility μ are of interest for this n-type semiconductor as they define the resistivity ρ and conductivity σ of the films as given by

$$\rho = \frac{1}{\sigma} = \frac{1}{eN\mu}. \quad (1)$$

In this equation, e is the elementary charge. A higher carrier density N not only increases the conductivity, but also decreases the light transmission of ZnO films by increasing the screened plasma frequency ω_{ps} below which transmission decreases

$$\omega_{ps}{}^2 = \frac{e^2}{\varepsilon_0 \varepsilon_r m^*} N, \quad (2)$$

where ε_0 is the vacuum permittivity, ε_r is the relative permittivity of ZnO (excluding the free-carrier contribution) at ω_{ps}, and m^* is the effective electron mass. Note that at ω_{ps} the real part of the dielectric function $\varepsilon_1 = 0$, which can be used to determine ω_{ps}. ω_{ps} furthermore relates to the unscreened plasma frequency ω_p in the Drude oscillator discussed in Sec. II.

The mobility μ is determined by various scattering processes, of which ionized-impurity scattering and grain-boundary scattering are the two most reported for ZnO.[2] Ionized-impurity scattering is caused by ionized dopant atoms (Al^+ in the case of aluminum-doped ZnO or Al:ZnO), which are introduced to provide additional free carriers but which can have a detrimental effect on μ due to this scattering. Grain-boundary scattering is caused by voids and unpassivated boundaries between the polycrystalline ZnO grains which provide electrical barriers for electron transport.[3,4] Note that even intrinsic ZnO (i-ZnO) usually has a significant carrier density, which is often attributed to hydrogen impurities present during growth (for simplicity we will continue to use the term i-ZnO even though it is technically not intrinsic).[5]

[a]Electronic mail: H.C.M.Knoops@tue.nl
[b]Electronic mail: M.Creatore@tue.nl

Insight into the scattering mechanisms in ZnO, and transparent conductive oxides (TCOs) in general, can be of great benefit for many applications. For transparent conductive oxides in solar cells, the approach is to limit the carrier density N to a certain value to keep ω_{ps} below the photon-energy range of interest for the specific solar cell. Therefore, a high mobility is desired for maximum conductivity and transparency. Note that various growth techniques which are available for ZnO can lead to large differences in terms of optical properties, electrical properties, and crystal structure. The relative scattering contributions as a result of these properties have to be determined to be able to optimize these growth techniques and thus the optical and electrical properties.

Two main methods to determine the scattering contributions can be distinguished: (1) Electrical measurements as a function of temperature: different scattering processes have different temperature dependencies, which can be used to identify scattering processes and additional information, such as the associated energy barriers. Four-point-probe (FPP), Hall, and other electrical measurements can be adopted.[2,6–10] (2) Comparing optical and electrical measurements: an advantage of optical measurements is that they are generally considered to be insensitive to grain-boundary scattering, and a comparison can therefore give insight into the grain-boundary contribution.[7,8,11–14] Optical techniques are noninvasive and contrary to method 1, require no change in temperature. Typically, the Drude oscillator is used to fit the optical properties in the infrared and near-infrared region.

Parameters from Drude oscillators are often used to determine the relative amount of grain-boundary scattering. However, since the Drude oscillator theoretically relates to all electron scattering processes, a physical interpretation of why grain-boundary scattering is not observed at optical frequencies (while it is detected by means of electrical measurements, i.e., low frequencies or constant current) is to our knowledge lacking in the previous reports, where the effect is used but not explained.[7,8,11–14] Furthermore, it is unclear what defines this frequency dependence or in which frequency range(s) it holds. Potentially, the Drude model would have to be adjusted to describe such a frequency dependence. Interestingly, in order to take into account a frequency dependence for ionized-impurity scattering, adjusted Drude models (denoted as Extended Drude models) are used in the literature.[15–18] Note that for ionized impurity scattering, the frequency above which scattering is observed to decrease is around ω_{ps}. A similar approach as taken for ionized-impurity scattering will be used in this work to develop a physical interpretation of the frequency-dependence of the Drude model.

To address the issues described in the previous paragraph, in this work plasma-deposited ZnO is characterized using spectroscopic ellipsometry (SE), Fourier-transform infrared spectroscopy (FTIR), and Hall measurements. For three case studies, data from both optical techniques are fitted using normal and Extended Drude models and the extracted parameters are compared to results from the Hall measurements to identify the scattering mechanisms. Finally, the concept of interaction distance is introduced to develop a physical interpretation of the relation between electron scattering and the Drude model for a wide photon energy range. This new physical interpretation provides a clear understanding of the applicability of Drude models in different frequency ranges, and can lead to new models such as the proposed Drude Multiscale model.

The article is set up as follows. First the basics and the assumptions in the Drude model are reviewed. Next, the experimental details are described and the modeling parameters are discussed. In Sec. IV A, a comparison of the models is presented to evaluate the different approaches and the obtained parameters for two case studies (i-ZnO and Al:ZnO, both with low grain-boundary scattering). A third case study involving a thickness series of Al:ZnO demonstrates how scattering mechanisms contributions can be separated. The concept of interaction distance is proposed and discussed in Sec. IV C, showing the benefits and the associated physical interpretation, leading to the Drude Multiscale model.

II. THEORY OF DRUDE MODELS AND FREQUENCY DEPENDENCE

Free-carrier absorption in metals and semiconductors is typically modeled by a Drude oscillator. Since the Drude model has an important role in this work, its fundamentals and assumptions are briefly discussed in this section.

The contribution of the Drude oscillator to the complex dielectric function ε is given by

$$\varepsilon(\omega) = -\frac{{\omega_p}^2}{\omega^2 + i\omega\omega_\tau}, \tag{3}$$

in which ω is the photon energy or frequency, ω_p is the unscreened plasma frequency, and ω_τ is the scattering or damping frequency (typically the Drude oscillator is used with the unscreened instead of the screened plasma frequency, to separate the interband contributions from the free-electron contribution). Note that in this work frequencies are expressed in units of eV, while formally they should be expressed in units of eV/$\hbar$.

When the effective electron mass m^* is known, the electron carrier density N and the electron mobility μ can be calculated directly from these parameters using the equations

$$N = \frac{\varepsilon_0 m^*}{e^2}{\omega_p}^2, \tag{4}$$

$$\mu = \frac{e}{m^*\omega_\tau}. \tag{5}$$

From the literature, it is known that m^* is approximately $0.28m_e$ for i-ZnO and 0.4–$0.5m_e$ for Al:ZnO (for carrier densities above $2\times10^{20}\,\mathrm{cm}^{-3}$), where m_e is the electron mass.[17,19]

For ionized-impurity scattering, ω_τ is only constant up to a certain transition frequency after which ω_τ decreases. This

transition frequency is typically near the screened plasma frequency ω_{ps}.[20] To incorporate the frequency dependence of ω_τ for ionized-impurity scattering, two models are generally used,[15] a semiempirical Extended Drude model,[16,17] or an empirical Extended Drude model.[18] In this work, we will use the semiempirical form to include the known power-law frequency dependence.[20] Equation (6) shows the used semiempirical form of ω_τ

$$\omega_\tau(\omega) = \frac{1}{1+\exp\frac{\omega-\omega_{tr}}{\sigma}}\omega_{\tau 0} + \left(1-\frac{1}{1+\exp\frac{\omega-\omega_{tr}}{\sigma}}\right)\omega_{\tau 1}\left(\frac{\omega}{\omega_{tr}}\right)^{\alpha}, \quad (6)$$

with $\omega_{\tau 0}$ as the low-frequency scattering frequency, $\omega_{\tau 1}$ as the high-frequency scattering frequency, ω_{tr} as the transition frequency, α as the power by which the high-frequency part changes ($\alpha = -3/2$ for ionized-impurity scattering),[20] and σ as the width of the transition region. This expression follows the expected physical behavior for ionized-impurity scattering as also shown by Mendelsberg *et al.*,[15] where ω_τ is roughly constant at a value of $\omega_{\tau 0}$ up to a transition frequency ω_{tr} after which it decreases with a power of 3/2.

Note that both Extended Drude forms reported in literature are not fully Kramers–Kronig (KK)-consistent. However, in practice, in most cases, the difference is small as it will be shown by comparisons with KK-consistent B-spline parameterizations in Sec. IV A. For this reason and for fast computation, the semiempirical Extended Drude model which is not fully KK-consistent is used in this work. Further physical interpretation of the Drude model and its frequency dependence will be discussed in Secs. IV C and IV D, where the interaction distance concept and the Drude Multiscale model will be proposed.

III. EXPERIMENTAL DETAILS

The i-ZnO and Al:ZnO films discussed in this work have been deposited using a plasma-enhanced chemical vapor deposition process. Previous publications described the deposition process in depth,[21–23] here only a brief overview is provided. The deposition tool consisted of an Ar-fed expanding thermal plasma where the deposition precursors [$Zn(C_2H_5)_2$, $Al(CH_3)_3$, and O_2] were fed into the downstream region at a pressure of 2 mbar. The substrates in the downstream region were heated to 200 °C. The growth rate ranged from 0.1 to 0.3 nm/s depending on the conditions. The $Zn(C_2H_5)_2$ flow rate was 9 g/h both for i-ZnO and Al:ZnO deposition and the $Al(CH_3)_3$ flow rate was 0.2 g/h in the case of Al:ZnO. Rutherford backscattering spectrometry measurements on the Al:ZnO showed no detectable carbon contamination and an Al content of 1.4 at. %.[23] The electrical resistance was measured by a FPP, and Hall measurements were performed on a Phystech RH 2010 to determine the carrier density and mobility. Single-side polished Si(100) substrates with 450 nm thermally grown SiO_2 on top were used to provide an insulating layer for the electrical measurements and for interference enhancement in the optical measurements.[24]

SE measurements were performed with a J.A. Woollam, Inc. M2000U (0.75–5.0 eV) ellipsometer and with a J.A. Woollam, Inc. M2000D (1.2–6.5 eV) on a variable angle stage. This range (0.75–6.5 eV) will be labeled in this work as the SE range. Ellipsometry measurements were performed at multiple angles of incidence (typically at 65°, 70°, 75°, 80°, and 85°). Reflectance FTIR measurements (0.05–0.87 eV) were performed at 12° incidence using a Bruker Tensor 27 with a reflectance unit. This range (0.05–0.87 eV) will be labeled as the FTIR range. The ellipsometry data and the reflectance FTIR data were fitted using the J.A. Woollam, Inc. CompleteEASE software. Note that reflection and ellipsometry data have been combined before in the literature,[25] but in this work the combination was performed to extend the photon-energy range of the dielectric function instead of improving the accuracy in the same photon-energy range. In the range covered by SE, the bare substrates (silicon with SiO_2) were fitted with the J.A. Woollam optical data library (a stack of SiO_2_JAW, INTR_JAW, and Si_JAW).[26] In the range covered by FTIR, general oscillator models of the substrates were fitted to measurements on the bare substrates. Due to negligible reflection from the rough backside of the Si wafer, the Si-wafer backside reflection was not taken into account in any of the analysis.

The ZnO was modeled as a homogeneous layer with a roughness layer. An effective medium approach (EMA) was used to model the surface roughness.[27] Note that ZnO layers that have large volume fractions (>2%) of depletion region (i.e., the space charge region around grain boundaries) should not be modeled as a homogeneous layer in the frequency ranges used in this work.[28] Those layers would typically have low doping levels and/or small grain sizes;[28] therefore, they would also be very different from the layers under investigation in this work.

To obtain the complex dielectric function, $\varepsilon_1 + i\varepsilon_2$, two approaches were used. In the first approach, a B-spline parameterized model was used to model the ZnO layers (only used in the SE range).[29,30] The KK-consistent mode was used for the B-splines with a node spacing of 0.1 eV and in the case of i-ZnO a higher node density (0.03 eV) was employed in the proximity of the band gap region. In the second approach, an oscillator model was used. The details of the optical modeling of both i-ZnO and Al:ZnO are described in Appendix A.

IV. RESULTS AND DISCUSSION

A. Case studies

In this section, three case studies are presented. For the first two cases, an 172 nm i-ZnO and a 555 nm Al:ZnO film were selected where grain-boundary scattering is expected to be low because: (1) the films have large grain sizes: ~90 nm for the i-ZnO film as deduced from SEM and atomic force microscopy (AFM) measurements (not shown here) and >150 nm for the Al:ZnO film as reported in a previous work,[23] and (2) the films have relatively low resistivity

values (as will be shown in Tables I and II). The third case treats a thickness series with a changing contribution of grain-boundary-scattering due to a development in grain size with film thickness as deduced from SEM measurements.[23] For the first two cases, Drude model fits of both SE and FTIR data are compared with B-spline parameterizations in terms of dielectric function in the range of 0.5–2.0 eV. B-spline parameterizations can be interpreted as a direct representation of the real dielectric function, since the B-spline is KK-consistent and is flexible enough to fit closely to the raw ellipsometry data for the different angles. As an example, the fits to the ellipsometry data at 85° angle of incidence are shown in the supplementary material (Fig. S1).[31] The obtained Drude parameters are discussed in conjunction with results from electrical measurements. The validity and interpretation of the fits and resulting parameters are discussed.

1. Case study: i-ZnO

To compare the various Drude fits for i-ZnO, a film of 172 nm thickness with 25 nm EMA roughness was used. Note that, due to the low carrier density of the i-ZnO film, the free-carrier contribution to the dielectric function is low and optical modeling of this contribution will be challenging. Therefore, also a relatively wide B-spline node spacing of 0.7 eV was chosen in this range to avoid oscillations, and since the transition frequency for ionized-impurity scattering is outside the range covered by SE, no Extended Drude model was applied in the SE range. When the Extended Drude model was applied to the reflection data in the FTIR range, the fit resulted to be not unique. We attribute this to the fact that reflection data are less sensitive to small changes in the dielectric function than SE data. Therefore, a normal Drude model was applied in the FTIR range. Figure 1 shows a Drude and a B-spline fit in the SE range and a Drude fit in the FTIR range. ε_1 is similar for all models on this scale, while ε_2 shows a difference between the models. Especially, the SE Drude modeling differs from the SE B-spline and FTIR Drude results.

Table I shows a comparison between the calculated electrical parameters from the two Drude fits and from Hall measurements. Interestingly, the carrier density is similar for all methods. Note that also ε_1 was similar for the two Drude fits, which can be explained by the fact that ε_1 relates strongly with the carrier density in the range where $\omega > \omega_\tau$. The expectation of a low contribution from grain-boundary-scattering implies

TABLE I. Electrical properties of an i-ZnO film obtained from Hall measurements, Drude modeling of FTIR reflection data, and Drude modeling of SE data. An m^* value of $0.28m_e$ was assumed to determine carrier density and carrier mobility. The uncertainty is indicated for the first value in each column.

Technique	Resistivity (10^{-3} Ω cm)	Carrier density (10^{19} cm^{-3})	Carrier mobility (cm^2/V s)
Hall	8 ± 1	2.6 ± 0.3	30 ± 1
FTIR Drude	7	3.1	31
SE Drude	11	3.3	18

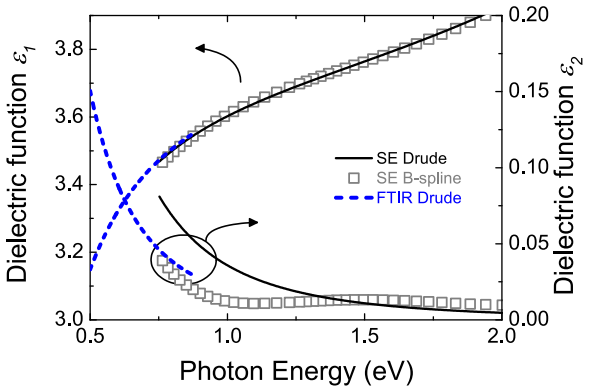

FIG. 1. (Color online) Dielectric function, $\varepsilon_1 + i\varepsilon_2$, for a 172 nm thick i-ZnO film in the photon energy range (0.5–2.0 eV). A Drude model and a B-spline parameterization of SE data and a Drude model of FTIR reflection data are shown.

agreement between the optical and Hall mobility. The mobility from the FTIR fit agrees with the mobility from the Hall measurement. The mobility value for the Drude oscillator fit in the SE range is different from both Hall and FTIR results which can be related to the fact that ε_2 was also different from the ε_2 derived from the B-spline and FTIR fit. To summarize, for this i-ZnO case, fits of data obtained in the FTIR or SE range can be used to obtain the carrier density, while only a fit of data obtained in the FTIR range can provide information on the optical mobility. In Secs. IV C and IV D, the applicability of FTIR and SE for optical mobility measurements will be discussed further.

2. Case study: Al:ZnO

To compare the various Drude fits for Al:ZnO, a film of 555 nm thickness with 37 nm EMA roughness was used. Figure 2 shows Drude, Extended Drude, and B-spline fits in the SE range and a Drude fit in the FTIR range. Due to the high carrier density of the Al:ZnO sample (as will be shown in Table II), the free-carrier contribution is strong in both the SE and FTIR range. For all fits in Fig. 2, the ε_1 results are very similar. However, in ε_2, a clear difference can be seen. The SE Drude deviates from the SE Extended Drude, the

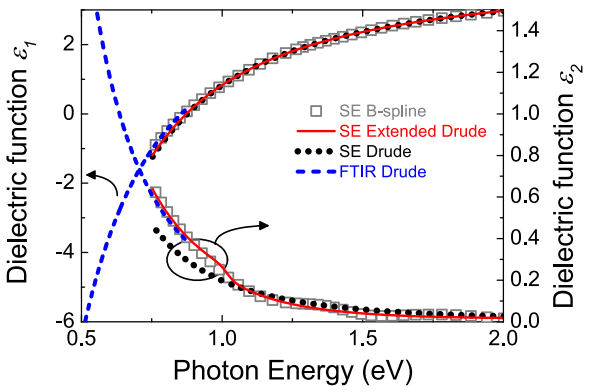

FIG. 2. (Color online) Dielectric function, $\varepsilon_1 + i\varepsilon_2$, for a 555 nm thick Al:ZnO film in the photon energy range (0.5–2.0 eV). A Drude model, an Extended Drude model, and a B-spline parameterization of SE data and a Drude model of FTIR reflection data are shown.

TABLE II. Electrical properties of a 555 nm thick Al:ZnO film obtained from Hall measurements, Drude modeling of FTIR reflection data, and Drude and Extended Drude modeling of SE data. An m^* value of $0.4m_e$ was assumed to determine carrier density and carrier mobility. The uncertainty is indicated for the first value in each column.

Technique	Resistivity (10^{-4} Ω cm)	Carrier density (10^{20} cm^{-3})	Mobility (cm^2/V s)
Hall	2.8 ± 0.1	7.5 ± 0.2	30 ± 1
FTIR Drude	2.9	7.5	29
SE Drude	2.2	7.6	38
SE Extended Drude	2.8	7.8	28

B-spline and the FTIR Drude, which all agree with each other. Note, furthermore, that the transition in the Extended Drude occurs around ω_{ps} (the region where $\varepsilon_1 = 0$), which corroborates the assumption that the transition for ionized impurity scattering should take place around ω_{ps}. The deviation of the SE Drude can therefore be ascribed to the fact that the transition for ionized impurity scattering is not taken into account in the normal Drude model.

Using an m^* value of $0.4m_e$, the Drude oscillator parameters were converted in electrical parameters and compared to Hall measurements as shown in Table II. When comparing the Drude models with the Hall measurements, similarly to the i-ZnO case, a good agreement for the carrier density is observed, which can be explained by the good agreement between ε_1 in the fits (note again that ε_1 links strongly to N in the range where $\omega > \omega_\tau$). The mobility values also show good agreement as expected because of the low contribution from grain-boundary scattering, except for the SE Drude fit, which also showed a poor correspondence in the ε_2 part. The mobility obtained from the Drude oscillator fit in the IR range shows that authors using a normal Drude model can still obtain the in-grain mobility when they include photon energies below the transition frequency in their fitting range.[11,32] The SE Drude fit shows that this does not hold when the range below the transition frequency is relatively narrow compared to the entire range used for fitting. To summarize, for this Al:ZnO case, fits of data obtained in the FTIR or SE range can be used to obtain an estimate on the carrier density and optical mobility. However, for the SE range, an Extended Drude model should be used.

3. Case study: Thickness series Al:ZnO

In chemical vapor deposition (CVD) growth of ZnO, a development in grain size with thickness is often observed. This development leads to a high contribution of grain-boundary scattering at low thicknesses, when grains are small, and a decreased contribution of grain-boundary scattering at higher thicknesses, when grains are larger. To investigate a case with such a transition, the same thickness series as reported by Ponomarev *et al.* of Al:ZnO deposited by plasma CVD[23] is used. Figure 3 shows the carrier density as determined by Hall measurements and Extended Drude model fits. The Extended Drude values have been scaled such that $N_{opt,avg} = N_{Hall,avg} = 7.3 \times 10^{20}$ cm^{-3} by adjusting

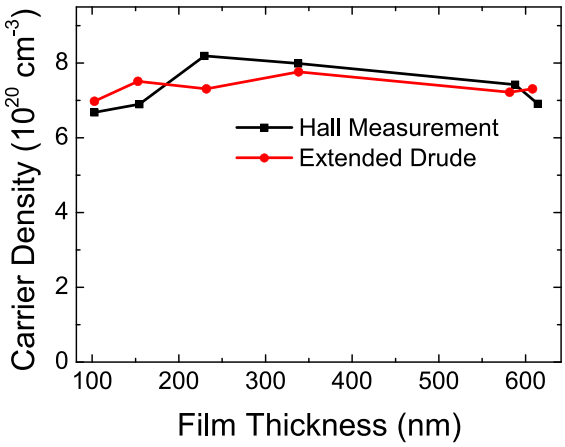

FIG. 3. (Color online) Carrier density as a function of thickness for Al:ZnO as determined by Hall measurements and Extended Drude modeling. For the Extended Drude modeling, an m^* value of $0.43m_e$ was used.

the value of m^*. This leads to a value for m^* of $0.43m_e$, which agrees well with the values found in literature (0.4–$0.5m_e$).[19] The relatively constant carrier density suggests a fairly homogeneous doping over the film thickness.

Using the calculated value of m^*, the carrier mobility can be determined. Figure 4 shows a comparison between the optical mobility as determined by the Extended Drude model and the Hall mobility. As it will be shown in Secs. IV C and IV D, the Extended Drude mobility can be assigned to the in-grain mobility and the Hall mobility can be assigned to the total mobility. In this case, the in-grain mobility is relatively constant with thickness, while the total mobility is initially low and increases up to the same level as the in-grain mobility with thickness. This behavior can be explained by a significant contribution of grain boundary scattering at low thicknesses and a negligible contribution at high thicknesses. To further quantify the relative importance of the different scattering mechanisms at different thicknesses, Sec. IV B will discuss a more intuitive approach to separate these processes.

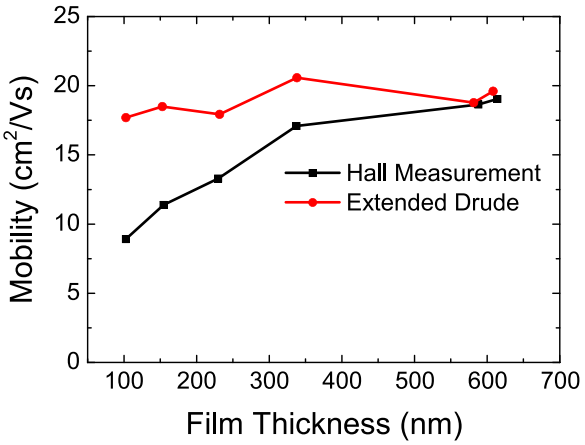

FIG. 4. (Color online) Carrier mobility as a function of thickness for Al:ZnO as determined by Hall measurements and Extended Drude modeling. For the Extended Drude modeling, an m^* value of $0.43m_e$ was used.

B. Determination of scattering processes

The previous comparison of mobility values as shown in Fig. 4 provides insight into the scattering processes. However, since mobility is inversely related to scattering, the separation into scattering processes is intuitively difficult. The interpretation becomes easier when using the scattering frequency ω_τ as a parameter for comparison, instead of mobility μ. The Drude model directly provides ω_τ and the following equation can be used for converting mobility values (for instance, from Hall measurements) into ω_τ values:

$$\omega_\tau = \frac{e}{m^*\mu}. \tag{7}$$

Interestingly, the inverse addition of mobility contributions $(1/\mu_{\text{tot}} = (1/\mu_1) + (1/\mu_2) + \ldots$, i.e., Matthiessen's rule) becomes a linear addition when scattering contributions are represented as ω_τ. Therefore, by considering that Hall measurements take into account all scattering processes, the determination of grain-boundary scattering versus optical mobility becomes simply

$$\omega_{\tau,\text{Hall}} = \omega_{\tau,\text{GB}} + \omega_{\tau,\text{Opt}}, \tag{8}$$

with $\omega_{\tau,\text{GB}}$ being the contribution to the scattering frequency from grain-boundary scattering and $\omega_{\tau,\text{Opt}}$ being the contribution to the scattering frequency by in-grain scattering (measured by optical techniques).

Furthermore, to distinguish between different in-grain scattering processes (splitting $\omega_{\tau,\text{Opt}}$ into its contributions), a simple estimate can be made of fundamental scattering processes. Note that here we consider all scattering processes that cannot be avoided as fundamental; therefore, this includes also ionized impurity scattering (since it cannot be avoided without changing the carrier density). A rough estimate of the fundamental scattering processes can be made by using the empirical Masetti model,[33] and the reported fitted curve as a function of the carrier density, as described by Ellmer.[34] The curve fitted by Ellmer can be taken as the maximum mobility that can be achieved for each carrier density. Using this function the minimum scattering frequency as a function of carrier density can be calculated. Here the fit parameters in their most recent work were used.[2] The difference between $\omega_{\tau,\text{Opt}}$ and this "fundamental" scattering contribution can be considered as caused by ineffective doping, defects and impurities. This contribution to the scattering is designated here by "other." These two contributions can replace $\omega_{\tau,\text{Opt}}$ in Eq. (8) and lead to the following equation:

$$\omega_{\tau,\text{Hall}} = \omega_{\tau,\text{GB}} + \omega_{\tau,\text{Fund}} + \omega_{\tau,\text{Other}}, \tag{9}$$

with $\omega_{\tau,\text{Fund}}$ as the fundamental contribution to the scattering frequency determined from the Masetti model and $\omega_{\tau,\text{Other}}$ as the other in-grain contributions to the scattering frequency.

The usefulness of this approach can be demonstrated using the thickness series of the previous case study as shown in Fig. 5, which addresses the different scattering contributions using Eqs. (8) and (9). The following observations can be made. (1) Since the carrier density is constant, the fundamental scattering $\omega_{\tau,\text{Fund}}$ is constant. (2) Since the in-grain mobility is fairly constant with thickness, the $\omega_{\tau,\text{Other}}$ contribution is also fairly constant. (3) For a film of 100 nm thickness, almost half of the scattering is attributed to grain boundaries. This contribution decreases as function of the film thickness, and for thick films (~600 nm), the contribution from grain-boundary scattering becomes negligible while most of the scattering processes are fundamental. If attempts would be made to improve the mobility of these films, then for the thin films the $\omega_{\tau,\text{GB}}$ component could be the main target for reduction, while a small improvement in mobility could be made for the thicker films by attempting to reduce the $\omega_{\tau,\text{Other}}$ contribution.

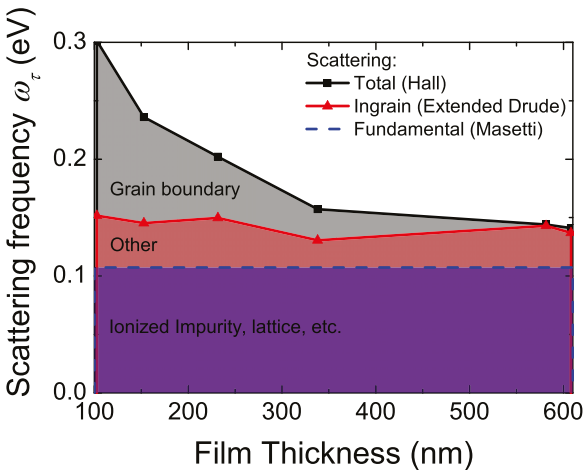

FIG. 5. (Color online) Scattering frequencies as a function of thickness for Al:ZnO as determined by Hall measurement, Extended Drude modeling, and the Masetti model. The differences between the total, in-grain, and fundamental scattering indicate the various physical scattering processes.

Another interesting case on which this approach can be used, is the comparison between scattering contributions in i-ZnO and Al:ZnO at the same thickness, as reported in Table III. Using the same procedure as above, the scattering contributions were determined for i-ZnO and compared to Al:ZnO at the same thickness of 172 nm. The i-ZnO values were obtained from the Hall and FTIR Drude mobility values from Table I, where m^* was adjusted to make the carrier density, as extracted from both methods, the same (as is the case for Al:ZnO). The Al:ZnO values were estimated for this

TABLE III. Comparison between i-ZnO and Al:ZnO of the absolute and relative scattering contributions at 172 nm thickness as defined by Eq. (9). The carrier densities are indicated and the used m^* values are $0.28m_e$ and $0.43m_e$, respectively.

		i-ZnO (2.6×10^{19} cm^{-3})		Al:ZnO (7.3×10^{20} cm^{-3})	
		Absolute (eV)	Fraction (%)	Absolute (eV)	Fraction (%)
Masetti	$\omega_{\tau,\text{Fund}}$	0.072	52	0.107	47
Grain boundaries	$\omega_{\tau,\text{GB}}$	0.018	13	0.081	36
Other	$\omega_{\tau,\text{Other}}$	0.049	35	0.039	17

thickness using Fig. 5. Due to the lower carrier density of i-ZnO, as expected, a lower fundamental contribution is observed in Table III (i.e., 0.072 eV vs 0.107 eV). However, note that due to the lower total scattering for i-ZnO, the fundamental scattering processes still contribute about half of the total scattering (i.e., 52%). The grain-boundary scattering for i-ZnO, is less than for the Al:ZnO case (i.e., 0.018 eV vs 0.081 eV). Two effects could be responsible: (1) the i-ZnO grains can be larger, which would be supported by the higher roughness, and (2) Al doping could form Al_2O_3 at grain boundaries, which would increase scattering in the Al:ZnO case. The "other" scattering processes represent a larger contribution to the total scattering processes for i-ZnO (i.e., 35% vs 17%). The approach to separate the scattering contributions, as shown in this section, demonstrates how insight into the factors limiting the mobility can be obtained by identifying these relative contributions.

C. Interaction distance

In this section, the results of the case studies and observations in the literature will be used to answer the questions from Sec. I on what defines the frequency dependency of the Drude model and in what frequency ranges different Drude models hold. To this end, a new concept, interaction distance, is developed to further facilitate the interpretation of results from optical modeling and predict which scattering processes contribute in different frequency ranges. Note that this concept has similarities with the approach on the effect of particle size for metal films as described by Kreibig and Vollmer.[41]

An implicit assumption in the Drude model is that the scattering probability does not depend on the location of the electron in the material. This assumption is not valid for grain-boundary scattering in ZnO during optical measurements. One basic assumption for the Drude model is that all electrons contribute equally to the Drude response. For grain-boundary scattering only the electrons localized near a grain boundary will scatter at the grain boundary during the measurement. The measured Drude response will not show grain boundary scattering since the majority of the electrons do not experience grain boundary scattering (negligible difference with a case without grain boundaries). This effect has been employed in the literature to separate grain-boundary scattering from other scattering mechanisms.[7,11,35] We have generalized this effect to the concept of *interaction distance* as shown schematically in Fig. 6(a). At the basis of this concept lies the following hypothesis: *The localization in space of scattering processes leads to a frequency dependence of the scattering frequency. An interaction distance between electrons and scattering centers can be defined dependent on photon energy and electron velocity. When the interaction distance is smaller than the distance between scattering centers for a specific scattering process, the contribution of the scattering process to the Drude oscillator is reduced.*

To be able to determine or estimate the interaction distance, several assumptions have to be made. First of all,

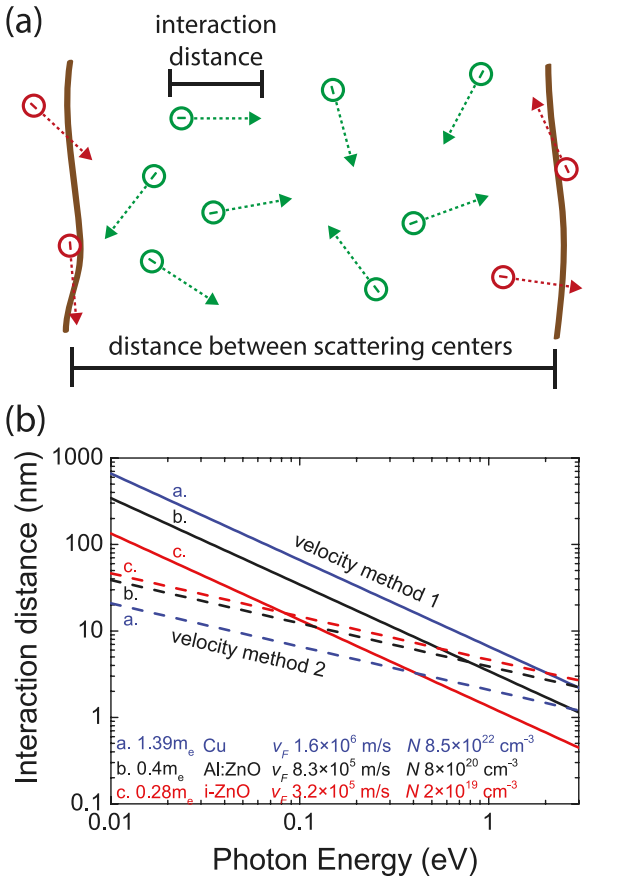

FIG. 6. (Color online) (a) Representation of the interaction distance concept. The path the electron travels during the interaction with a photon is indicated with an arrow, where the length of the arrow is the interaction distance. When the interaction distance is smaller than the distance between the scattering centers in question, a large part of the free electrons do not experience those scattering events. (b) Interaction distance as a function of photon energy according to Eq. (10) and for both velocity methods. Besides for Al:ZnO and i-ZnO also the results for Cu are indicated for comparison. The legend indicates effective mass m^*, Fermi velocity v_F, and carrier density N values for the shown materials. Note that the accuracy for low-doped films is expected to be lower than in the case of high doping.

following from the definition, the interaction distance of the electron, d_{int}, is the electron velocity, v_e, times the interaction time T_{int}. The interaction time is derived from the assumption that a photon is roughly localized in a volume with a size defined by the wavelength of the photon.[36] Assuming that the size of this localization volume determines the interaction time with the electron, and assuming that the electron velocity can be neglected with respect to the speed of light (otherwise the direction of the electron would play a role), then the interaction time becomes the reciprocal value of the light frequency, $T_{\text{int}} = 1/f = 2\pi/\omega$, which leads to the expression for the interaction distance

$$d_{\text{int}} = v_e T_{\text{int}} = v_e 2\pi/\omega. \tag{10}$$

Note that the mean free path (MFP) of the electron can be easily calculated in a similar way by the following equation:

$$\text{MFP} = v_e \tau = v_e/\omega_t, \tag{11}$$

where τ is the scattering time associated with the scattering process and which can be calculated from ω_τ by $\tau = 1/\omega_\tau$. Note that there is no factor of 2π in this relation because ω_τ is not an angular frequency. The MFP is not necessarily the same as the distance between scattering centers, because for the MFP also the scattering cross-section has to be taken into account. Therefore, the MFP will be an upper limit for the distance between scattering centers. For the average velocity of the electron, two approaches can be taken: (1) *The Fermi velocity*: due to the Pauli Exclusion Principle, electrons cannot scatter into occupied states. Therefore for degenerate semiconductors only electrons near the Fermi surface and with the Fermi velocity have to be taken into account [$v_F = \hbar(3\pi^2 N)^{1/3}/m^*$].[18] (2) *The electron velocity if the photon provides all the kinetic energy*: this is a rough estimate, which simplifies the calculation by assuming that all the energy in the photon is transferred to the electron as kinetic energy [$v_{\text{transfer}} = \sqrt{}(2\,\hbar\omega/m^*)$]. These two methods represent extremes where in method 1 the velocity is the same as if the electron did not interact with the light and in method 2 the maximum amount of energy transfer occurs, while the electron initially was at rest. Note that calculating the interaction distance using method 1 is similar to the standpoint of the Kubo linear response theory,[37] but the application of this theory is outside the scope of this paper. Figure 6(b) shows the calculated interaction distance as a function of photon energy for both methods, for both i-ZnO and Al:ZnO. The calculated lines for Cu are also added to serve as an example of a metal. In both velocity methods, d_{int} decreases with increasing ω, which fits with the expectation for this concept (e.g., scattering on grain boundaries of large grains is only observed in static or low frequency measurements). For the first case, the decrease goes by a factor of ω and in the second case by the square root of ω. Furthermore, materials with a higher Fermi velocity have a larger interaction distance in the case of method 1, while for method 2, the interaction distance is only affected by m^* [see legend Fig. 6(b)], where a lower m^* value results in a larger interaction distance. Note that the actual velocity could also be a combination of methods 1 and 2, where for Cu method 1 would provide the largest contribution and for i-ZnO method 2 would provide the largest contribution at high frequency.

The observation that grain-boundary scattering occurs outside the optical range can be tested against the trends in Fig. 6(b). Assuming a grain size of $\sim$100 nm, a transition photon energy of 0.04 eV can be found for Al:ZnO using method 1, which is just below the range covered by FTIR and therefore outside the optical range (in this work, the FTIR range is taken as the low-energy limit of the optical range). For i-ZnO, the transition occurs even at a lower energy because of the lower Fermi velocity. When method 2 is used for the velocity, the energy is even lower. For metals which have higher Fermi velocity the transition occurs at a higher energy but still at the boundary of the FTIR range. The interaction distance concept predicts that for all these materials, grain-boundary scattering would not be observed by FTIR or SE measurements, which corresponds with the observations in the case studies. Note that for smaller grain sizes, grain boundary scattering could have an influence in the FTIR range.

Similarly, the mean scattering time for ionized-impurity scattering can be tested. For Al:ZnO with a carrier density of $8 \times 10^{20}\,\text{cm}^{-3}$, a MFP between ionized-impurity scattering of 4.7 nm can be estimated using Eq. (11) using ω_τ derived from the Masetti model used in Sec. IV B. Assuming that the MFP is similar to the interaction distance a transition frequency of 0.7 eV is obtained using method 1 and a value of 0.67 eV using method 2 [Fig. 6(b)]. Both of these are relatively close to the transition frequency observed for the Extended Drude model in Fig. 2, which is around $\sim$1 eV and is close to ω_{ps}. For ionized-impurity scattering in i-ZnO an MFP of 3.3 nm is calculated which would give a transition energy of 0.4 eV for method 1 and of 2 eV using method 2. The large difference between the two methods is caused by the lower Fermi velocity and effective mass compared to Al:ZnO. Note that a Drude fit is in a sense a weighted average over the FTIR range with a stronger weight to low photon energies. Therefore, also a transition energy of 0.4 eV could result in an accurate in-grain mobility determination from a Drude fit in the FTIR range. In general, the interaction distance concept is in agreement with the observed transitions for ionized impurity scattering, which shows that the interaction distance concept can be used to explain both the frequency dependence of grain-boundary scattering and of ionized-impurity scattering.

A review of the frequency ranges reported for different scattering mechanisms in the literature, can provide further indication of the strength of the interaction distance concept and can show the application of the concept outside the optical range (e.g., in the megahertz and terahertz range). The following list discusses for each type of scattering center, examples of observations in the literature, and how they can be explained using the interaction distance concept: (1) Grain boundaries: Impedance spectroscopy on resistive ZnO has shown a transition above certain frequencies, which is in line with the concept described in this work.[38] Note that the effective electron velocity may be very low due to a low Fermi velocity and hopping transport via defects.[39] In general, therefore, the estimated interaction distance for lowly doped films suffers from a larger uncertainty. The transitions are generally in the kilohertz–megahertz range ($\sim 10^{-9}$ eV). Note that influence of grain boundary scattering has been reported even at higher frequency ranges in the case of large depletion regions around the grain boundaries.[28] In this case, the assumption of a homogeneous material cannot be used and an effective medium approach is required. Combining such an approach with the interaction distance concept is outside the scope of this work since it is not applicable to the model systems under investigation. (2) Ionized impurities: For ionized-impurity scattering, a decrease in scattering is seen above a certain transition energy. The value of the transition energy increases with carrier density,[40] which agrees with a smaller distance between the dopants. The transition is generally above the terahertz range (0.2–1 eV). (3) Defects, neutral impurities, etc.: In principle, a similar effect as for ionized impurity scattering should be present although

these other defects and impurities constitute a smaller fraction of the scattering in most ZnO materials and a frequency dependence is therefore less studied and not reported. (4) Scattering processes that do not depend on the position of the electron (e.g., phonon scattering). These processes will play a role at all length scales and are not expected to show a frequency dependence.

The interaction distance concept can also explain observations from metallic materials. Metals generally have high Fermi velocities compared to TCOs, and therefore, the interaction distance will be larger than the distance between scattering centers for most photon energies [as shown for Cu in Fig. 6(b)]. Therefore, resistivity values obtained from optical modeling of metallic films generally agrees with electrical measurements. In the case of nanoparticles, scattering at particle boundaries becomes important and has to be taken into account. A variety of approaches to take this scattering into account exist such as described by Kreibig and Vollmer,[41] and by the Drude–Smith model.[42] Interestingly, the effect on the dielectric function with the Drude–Smith model is similar as in our approach (i.e., higher scattering at low frequencies), and therefore, our model might be applicable in those situations as well.

D. Drude Multiscale

To integrate the interaction distance concept into the Drude model, a new general frequency-dependent Drude model can be defined. The interaction distance concept can be used to define a frequency dependent $\omega_\tau(\omega)$ based on the frequency independent ω_τ from Eq. (9). This $\omega_\tau(\omega)$ then consists of all the different scattering contributions in a material at different length scales and can be used directly in the Drude model from Eq. (3). This $\omega_\tau(\omega)$ would then be a summation of functions for the separate contributions

$$\omega_\tau(\omega) = \omega_{\tau,\mathrm{GB}}(\omega, T_{\mathrm{GB}}, s_{\mathrm{GB}}) + \omega_{\tau,\mathrm{ii}}(\omega, T_{\mathrm{ii}}, s_{\mathrm{ii}}) + \omega_{\tau 0}. \quad (12)$$

Here, only the grain-boundary contribution $\omega_{\tau,\mathrm{GB}}$ and the ionized-impurity contribution $\omega_{\tau,\mathrm{ii}}$ are included as frequency-dependent contributions, although more could be added. $\omega_{\tau 0}$ is the contribution that does not depend on frequency. Parameters such as transition energy (T) and transition width (s) can be defined for each contribution. The transition energy would depend on the average distance between scattering centers and the transition width would depend on the spread in the distance between scattering centers. For grain-boundary scattering, this spread could be related to a variation in grain size and for ionized-impurity scattering to a variation in dopant distance. In case $\omega_\tau(\omega)$ has a strong dependence on ω it is important to ensure KK-consistency. The frequency-dependent Drude model can be made KK-consistent by ensuring that $\omega_\tau(\omega)$ is KK-consistent as shown in Appendix B [Eq. (B4)]. Such a Drude would be valid at many length scales and therefore we label it a "Drude Multiscale" model. Figure 7 provides a graphical overview of the Drude Multiscale concept applied to Al:ZnO from the case studies. Besides showing which scattering mechanisms play a role and in which frequency ranges, the model also explains why specific Drude models can be used in specific ranges. Note that the Drude Multiscale model in principle can also be applied outside of the optical range, such as terahertz spectroscopy and impedance spectroscopy.

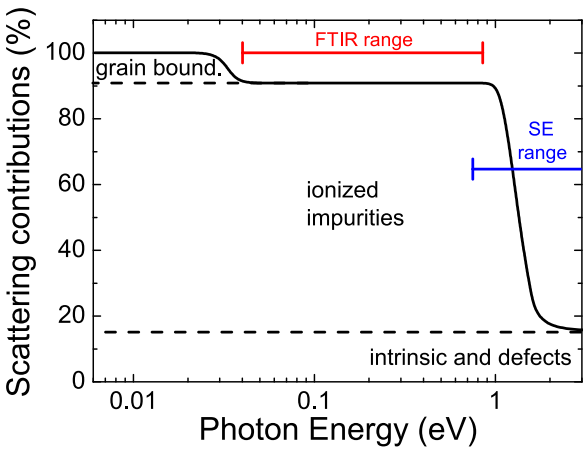

FIG. 7. (Color online) Overview of $\omega_\tau(\omega)$ as a function of photon energy for Al:ZnO. The decrease in $\omega_\tau(\omega)$ shows where certain scattering contributions disappear. The ranges where the normal Drude (FTIR range) or the Extended Drude (SE range) can be used are indicated.

Applying this view to effects observed in the case studies, the following can be concluded. Drude models fitted to optical data do not show grain-boundary scattering because the latter does not contribute at those length scales. Normal Drude models can only be used to obtain the in-grain mobility in the case that the contribution from ionized impurity scattering is high in the used photon energy range (when for a significant part of the range $\varepsilon_1 < 0$). Otherwise the obtained mobility will not or only partially include ionized-impurity scattering. Note, that for fitting to ε_1 in the range where $\omega > \omega_\tau$, the obtained carrier density is still correct. Therefore, a valid method to determine the total mobility is to determine the total resistivity using FPP and to calculate the total mobility using Eq. (1) using the carrier density value as derived from SE.

V. CONCLUSIONS

In this work, a novel view on the relation between various Drude optical models and scattering processes was presented. Using the concept "interaction distance," a physical interpretation of why Drude models do not observe grain boundary scattering and a guideline as in what frequency ranges Drude models can be used was obtained. For instance, for i-ZnO the in-grain mobility was obtained by fitting reflection data in the IR photon-energy range with a normal Drude model; and for Al:ZnO both a normal Drude fit in the IR range or an Extended Drude fit in the range covered by SE could be used to obtain the in-grain mobility. To provide more insight into contributions of various scattering mechanisms the parameter "scattering frequency" was used instead of mobility. Using this parameter, scattering mechanisms for a thickness series of Al:ZnO were separated in the contributions originating from grain-boundary scattering, ionized impurity scattering, and other scattering mechanisms. In general, understanding

the interaction distance concept allows the prediction of which Drude models can be used in what frequency range and how these models can be used to determine scattering contributions. This view furthermore opens up the possibility to use new Drude models which integrate frequency dependence such as a Drude Multiscale model.

ACKNOWLEDGMENTS

N. Leick, B. Platier, and Y. G. Melese are gratefully acknowledged for their contribution to this work. This work was financially supported by Interreg Vlaanderen Nederland, Solar flare under Project No. IVA-VLANED-1.59. The authors thank, also for the financial support, the Ministry of Economical Affairs, *Pieken in de Delta Zuid-Oost* (*project CIGSelf Verbeteren*). The research of M.C. has been funded by the Netherlands Organization for Scientific Research (NWO, *Aspasia programma*).

APPENDIX A

In this section, the details of the optical modeling of the dielectric function are described as are the resulting fits and fit parameters. The dielectric functions for the oscillator models for i-ZnO and Al:ZnO had the following form:

$$\varepsilon = \varepsilon_\infty + \varepsilon_{\text{interband}} + \varepsilon_{\text{Gauss}} + \varepsilon_{\text{Drude}}, \tag{A1}$$

where ε_∞ is a constant, used to correct for higher-energy contributions, $\varepsilon_{\text{interband}}$ is an oscillator with a band gap to account for interband absorption, $\varepsilon_{\text{Gauss}}$ is a Gaussian oscillator to account for near-bandgap absorption, and $\varepsilon_{\text{Drude}}$ is the Drude oscillator as discussed in Sec. II. Phonon contributions were not included since these were outside of the range considered in this work. In the case of i-ZnO, the $\varepsilon_{\text{interband}}$ contribution is described by an oscillator with a sharp onset, which is the PSEMI-M0 model.[43] The PSEMI-M0 oscillator consists of four polynomial spline functions connected end-to-end, controlled by the following fit parameters: *Amp*, which controls the amplitude of the oscillator; *Br*, which controls the broadening; *Eo*, which controls the oscillator peak energy; *WR*, which controls the distance between *Eo* and the right end point; *PR*, which controls the position of the control point on the right of the center peak; *AR*, which controls the amplitude of this control point; and *O2R*, which controls the shape around this control point. In the case of Al:ZnO a softer absorption onset allows the use of a Tauc–Lorentz oscillator for $\varepsilon_{\text{interband}}$,[44] with the form:

$$\varepsilon_2 = \begin{cases} \dfrac{1}{\hbar\omega}\dfrac{AE_0B(\hbar\omega - E_g)^2}{[(\hbar\omega)^2 - E_0{}^2]^2 + B^2(\hbar\omega)^2}, & \hbar\omega > E_g \\ 0, & \hbar\omega \le E_g, \end{cases} \tag{A2}$$

where A, E_0, E_g, and B are the fit parameters. ε_1 is determined by KK-conversion of ε_2. For the Gaussian oscillator, ε_2 had the following form:

$$\varepsilon_2 = A\left(e^{-4\ln 2\left(\frac{\hbar\omega - E_0}{B}\right)^2} - e^{-4\ln 2\left(\frac{\hbar\omega - E_0}{B}\right)^2}\right), \tag{A3}$$

where A, E_0, and B are the fit parameters. ε_1 is again determined by KK-conversion of ε_2.

In Fig. 8, a comparison between the dielectric functions, as derived by the B-spline approach and the oscillator model from Eq. (A1), are shown for a 209.7 nm i-ZnO film with 29.8 nm EMA roughness and a 203.9 nm Al:ZnO film with 27.9 nm EMA roughness. Table IV shows the fitted parameters of the used oscillator models. Overall, the dielectric functions from the B-spline parameterizations show fairly good agreement with the dielectric functions from the oscillator models. The transparent region of ZnO up to the band gap at ~3.3 eV is observed. The combined effect of the Burstein–Moss shift and bandgap narrowing results in a higher band gap of the interband absorption for Al:ZnO than for i-ZnO, as observed from the shift to higher photon energies.[45–47] Furthermore, for Al:ZnO the excitonic transition above the band gap broadens due to screening by free electrons.[44] This broadening causes a softer absorption onset at the bandgap region compared to i-ZnO, which allows the use of the Tauc–Lorentz oscillator [Eq. (A2)]. The B-spline and oscillator model show differences for higher photon energies (≳4 eV) especially for i-ZnO, which can be explained by depolarization due to roughness, since the measured depolarization data (not shown) show a higher depolarization for this range.[48] The larger roughness for i-ZnO is confirmed by the RMS roughness measured by AFM which is 18 nm for i-ZnO compared to 12 nm for Al:ZnO. Note that the SE modeled roughness (respectively, 30 and 28 nm) is generally higher than the AFM roughness.[27]

Table IV shows that for i-ZnO the uncertainty in the Drude oscillator parameters is very large when fitted in the SE data range, which can be explained by a strong correlation between the Drude oscillator parameters. By fitting the Drude oscillator parameters in the FTIR reflection data range, a weak correlation between the parameters is achieved and these can therefore be fitted with more confidence. Figure 9 shows an example of the FTIR reflection data for a different set of i-ZnO and Al:ZnO films, which are relatively thick. Only the Drude oscillator parameters are fitted in the range covered by FTIR, while the parameters for

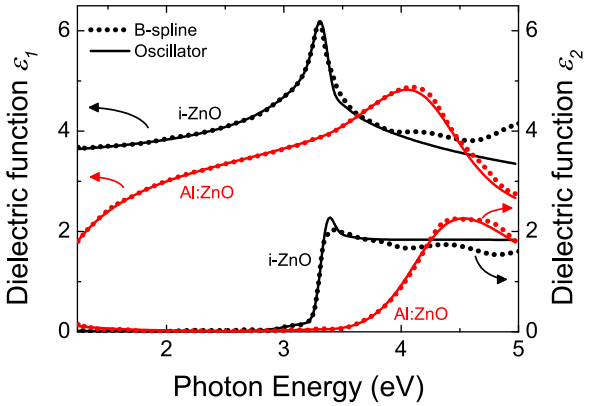

FIG. 8. (Color online) Dielectric function, $\varepsilon_1 + i\varepsilon_2$, as a function of photon energy for i-ZnO (209.7 nm) and Al:ZnO (203.9 nm). The oscillator-based models are indicated by solid lines and the B-spline parameterizations by dotted lines.

TABLE IV. Fitted parameters of the general oscillator model for i-ZnO and Al:ZnO. The oscillators are indicated and the uncertainty margins as provided by the CompleteEASE software are included. Note that the Drude oscillator contribution for i-ZnO has strongly correlated parameters in this photon range, and therefore has a large uncertainty.

	i-ZnO	Al:ZnO
Thickness (nm)	209.7 ± 0.2	203.9 ± 0.3
EMA roughness (nm)	29.8 ± 0.1	27.9 ± 0.2
Oscillator parameters	$\varepsilon_\infty = 0.7 \pm 0.2$	$\varepsilon_\infty = 2.97 \pm 0.02$
	$\varepsilon_{\text{PSEMI}}$	ε_{TL}
	$Amp = 9 \pm 5$	$A = 51 \pm 2$ eV
	$Br = 0.062 \pm 0.003$ eV	$B = 1.21 \pm 0.04$ eV
	$Eo = 3.341 \pm 0.007$ eV	$E_o = 4.29 \pm 0.01$ eV
	$WR = 58 \pm 1$ eV	$E_g = 3.37 \pm 0.02$ eV
	$PR = 0.999 \pm 0.001$	
	$AR = 0.2 \pm 0.1$	
	$O2R = -1.0 \pm 0.5$	
	$\varepsilon_{\text{Gauss}}$	$\varepsilon_{\text{Gauss}}$
	$A = 0.17 \pm 0.01$	$A = 0.05 \pm 0.01$
	$B = 0.51 \pm 0.03$ eV	$B = 1.0 \pm 0.2$ eV
	$E_0 = 3.25 \pm 0.03$ eV	$E_0 = 3.6 \pm 0.2$ eV
	$\varepsilon_{\text{Drude}}$	$\varepsilon_{\text{Drude}}$
	$\omega_p = 1 \pm 25$ eV	$\omega_p = 1.678 \pm 0.003$ eV
	$\omega_\tau = 46 \pm 2260$ eV	$\omega_\tau = 0.080 \pm 0.001$ eV

contributions at higher photon energy are kept fixed. For i-ZnO, the expected interference oscillation resulting from the interference in both the ZnO layer and the 450 nm SiO_2 layer from the substrate is observed (note that, a small peak above 0.1 eV is visible, which is the transversal optical mode of Si-O at 1075 cm^{-1}).[49] Due to the high carrier concentration of Al:ZnO, no interference oscillation is seen in this case, but instead a metal-like reflection is observed. Note, that in the IR range only the properties of the top ~250 nm will have an influence for doped ZnO due to absorption (assuming a detection limit of 0.001 of the total reflected light). For simplicity, in this work the 0.2–0.87 eV range is chosen for the fitting of the Drude oscillator parameters. By this choice the energy range below 0.2 eV where various phonon modes can be present is avoided,[50] and the material also does not have to be modeled as an EMA as long as volume fractions of the depletion region are below 2%.[28]

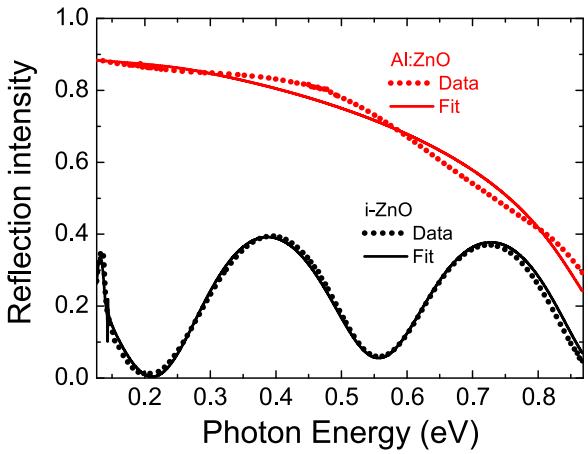

FIG. 9. (Color online) Infrared reflection intensity data and fits as a function of the photon energy for a 541 nm Al:ZnO film and a 629 nm i-ZnO film determined by reflection FTIR.

APPENDIX B

In this section, KK-consistent forms of frequency-dependent Drude models are presented. KK-consistent forms of these models were developed to make these models applicable for cases where non-KK-consistent forms fail. This could be an issue when ω_τ is large compared to ω and when also ω_τ changes strongly as a function of ω. KK-consistent forms of these models can be defined by using a Hilbert transform. When the Hilbert transform $H\{f(\omega)\}(\omega)$ of the real part of $\omega_\tau(\omega)$ is known, an equation for $\omega_\tau(\omega)$ can be defined which will automatically give a KK-consistent Drude model

$$\omega_\tau(\omega) = A[F(\omega) + iH\{F(\omega)\}(\omega)], \tag{B1}$$

where A is a part that does not depend on ω, and $F(\omega)$ is an even and real function of ω. An example is an expression using the arctan function, which is similar to the empirical Extended Drude model in the literature[51]

$$F(\omega;T,s) = \frac{1}{\pi}\left[\arctan\left(\frac{\omega+T}{s}\right) - \arctan\left(\frac{\omega-T}{s}\right)\right], \tag{B2}$$

$$H\{F(\omega;T,s)\}(\omega) = \frac{1}{\pi}\operatorname{arctanh}\left(\frac{2\omega T}{\omega^2+T^2+s^2}\right), \tag{B3}$$

with T the transition frequency and s the transition width. This form has a very soft transition, which might not be flexible enough to fit all experimental transitions in ω_τ. These or similar forms for $\omega_\tau(\omega)$ can also be added together while maintaining KK-consistency. Therefore, Matthiesen's rule for adding scattering contributions [Eq. (9)] can be used to define a new $\omega_\tau(\omega)$ [similar to Eq. (12)]

$$\omega_\tau(\omega) = \omega_{\tau 0} + \sum_{i=1}^{\infty} \omega_{\tau i}[F_i(\omega;T_i,s_i) + iH\{F_i(\omega;T_i,s_i)\}(\omega)], \tag{B4}$$

where T_i and s_i can be used as parameters such as transition energy and transition width for each contribution. The transition energy would depend on the average distance between scattering centers and the transition width would depend on the spread in the distance between scattering centers. This $\omega_\tau(\omega)$ can be inserted in Eq. (3) to obtain a KK-consistent frequency-dependent Drude model.

[1]K. Ellmer, Nat. Photonics **6**, 809 (2012).
[2]K. Ellmer and R. Mientus, Thin Solid Films **516**, 4620 (2008).
[3]J. Y. W. Seto, J. Appl. Phys. **46**, 5247 (1975).
[4]G. Baccarani, B. Riccò, and G. Spadini, J. Appl. Phys. **49**, 5565 (1978).
[5]A. Janotti and C. G. Van de Walle, Rep. Prog. Phys. **72**, 126501 (2009).
[6]D. L. Young, T. J. Coutts, V. I. Kaydanov, A. S. Gilmore, and W. P. Mulligan, J. Vac. Sci. Technol., A **18**, 2978 (2000).
[7]S. Faÿ, J. Steinhauser, S. Nicolay, and C. Ballif, Thin Solid Films **518**, 2961 (2010).

[8]J. J. Robbins, J. Harvey, J. Leaf, C. Fry, and C. A. Wolden, Thin Solid Films **473**, 35 (2005).
[9]A. Leenheer, J. Perkins, M. van Hest, J. Berry, R. O'Hayre, and D. Ginley, Phys. Rev. B **77**, 115215 (2008).
[10]R. V. Muniswami Naidu, A. Subrahmanyam, A. Verger, M. K. Jain, S. V. N. Bhaskara Rao, S. N. Jha, and D. M. Phase, J. Electron. Mater. **41**, 660 (2012).
[11]J. Steinhauser, S. Faÿ, N. Oliveira, E. Vallat-Sauvain, and C. Ballif, Appl. Phys. Lett. **90**, 142107 (2007).
[12]I. Volintiru, M. Creatore, and M. C. M. van de Sanden, J. Appl. Phys. **103**, 033704 (2008).
[13]T. Yamada, H. Makino, N. Yamamoto, and T. Yamamoto, J. Appl. Phys. **107**, 123534 (2010).
[14]K. Sago, H. Kuramochi, H. Iigusa, K. Utsumi, and H. Fujiwara, J. Appl. Phys. **115**, 133505 (2014).
[15]R. J. Mendelsberg, G. Garcia, and D. J. Milliron, J. Appl. Phys. **111**, 063515 (2012).
[16]A. Pflug, V. Sittinger, F. Ruske, B. Szyszka, and G. Dittmar, Thin Solid Films **455**, 201 (2004).
[17]F. Ruske, A. Pflug, V. Sittinger, B. Szyszka, D. Greiner, and B. Rech, Thin Solid Films **518**, 1289 (2009).
[18]N. Ehrmann and R. Reineke-Koch, Thin Solid Films **519**, 1475 (2010).
[19]W. M. Kim, I. H. Kim, J. H. Ko, B. Cheong, T. S. Lee, K. S. Lee, D. Kim, and T.-Y. Seong, J. Phys. D: Appl. Phys. **41**, 195409 (2008).
[20]I. Hamberg and C. G. Granqvist, J. Appl. Phys. **60**, R123 (1986).
[21]R. Groenen, J. Lo, J. L. Linden, R. E. I. Schropp, and M. C. M. Van De Sanden, Thin Solid Films **492**, 298 (2005).
[22]I. Volintiru, M. Creatore, B. J. Kniknie, C. I. M. A. Spee, and M. C. M. van de Sanden, J. Appl. Phys. **102**, 043709 (2007).
[23]M. V. Ponomarev, M. A. Verheijen, W. Keuning, M. C. M. van de Sanden, and M. Creatore, J. Appl. Phys. **112**, 043708 (2012).
[24]W. A. McGahan, B. Johs, and J. A. Woollam, Thin Solid Films **234**, 443 (1993).
[25]I. An, H. V. Nguyen, A. R. Heyd, and R. W. Collins, Rev. Sci. Instrum. **65**, 3489 (1994).
[26]C. M. Herzinger, B. Johs, W. A. McGahan, J. A. Woollam, and W. Paulson, J. Appl. Phys. **83**, 3323 (1998).
[27]H. Fujiwara, J. Koh, P. Rovira, and R. Collins, Phys. Rev. B **61**, 10832 (2000).
[28]P. Prunici, F. U. Hamelmann, W. Beyer, H. Kurz, and H. Stiebig, J. Appl. Phys. **113**, 123104 (2013).
[29]B. Johs and J. S. Hale, Phys. Status Solidi A **205**, 715 (2008).
[30]J. W. Weber, T. A. R. Hansen, M. C. M. van de Sanden, and R. Engeln, J. Appl. Phys. **106**, 123503 (2009).
[31]See supplementary material at http://dx.doi.org/10.1116/1.4905086 for fits of the ellipsometry data of Fig. 2.
[32]C. David, T. Girardeau, F. Paumier, D. Eyidi, B. Lacroix, N. Papathanasiou, B. P. Tinkham, P. Guérin, and M. Marteau, J. Phys.: Condens. Matter **23**, 334209 (2011).
[33]G. Masetti, M. Severi, and S. Solmi, IEEE Trans. Electron Devices **30**, 764 (1983).
[34]K. Ellmer, J. Phys. D: Appl. Phys. **34**, 3097 (2001).
[35]J. Steinhauser, S. Faÿ, N. Oliveira, E. Vallat-Sauvain, D. Zimin, U. Kroll, and C. Ballif, Phys. Status Solidi A **205**, 1983 (2008).
[36]B. J. Smith and M. G. Raymer, New J. Phys. **9**, 414 (2007).
[37]M. Le Bellac, F. Mortessagne, and G. G. Batrouni, *Equilibrium and Non-Equilibrium Statistical Thermodynamics* (Cambridge University, Cambridge, 2004).
[38]S. Mandal, H. Mullick, S. Majumdar, A. Dhar, and S. K. Ray, J. Phys. D: Appl. Phys. **41**, 025307 (2008).
[39]V. Gupta and A. Mansingh, Phys. Rev. B **49**, 1989 (1994).
[40]B. E. Sernelius and M. Morling, Thin Solid Films **177**, 69 (1989).
[41]U. Kreibig and M. Vollmer, *Optical Properties of Metal Clusters*, Materials Science (Springer, Berlin, Heidelberg, 1995), Vol. 25.
[42]N. Smith, Phys. Rev. B **64**, 155106 (2001).
[43]T. Tiwald, "PSEMI" Oscillator Model (Woollam Co. News) (2006), pp. 6–7.
[44]H. Fujiwara and M. Kondo, Phys. Rev. B **71**, 075109 (2005).
[45]A. Jain, P. Sagar, and R. M. Mehra, Solid-State Electron. **50**, 1420 (2006).
[46]J. G. Lu *et al.*, J. Appl. Phys. **101**, 083705 (2007).
[47]A. Abdolahzadeh Ziabari and S. M. Rozati, Phys. B **407**, 4512 (2012).
[48]K. H. Jun, J. H. Kwak, and K. S. Lim, J. Opt. Soc. Am. A **20**, 1060 (2003).
[49]V. Tolstoy, I. Chernyshova, and V. Skryshevsky, *Handbook of Infrared Spectroscopy of Ultrathin Films* (Wiley, New York, 2003), p. 710.
[50]C. Bundesmann, R. Schmidt-Grund, M. Schubert, K. Ellmer, A. Klein, and B. Rech, *Transparent Conductive Zinc Oxide*, Materials Science, edited by K. Ellmer, A. Klein, and B. Rech (Springer, Berlin, Heidelberg, 2008), Vol. 104, pp. 79–124.
[51]D. Mergel and Z. Qiao, J. Phys. D: Appl. Phys. **35**, 794 (2002).